Front propagation and pattern formation of Taylor vortices growing into unstable circular Couette flow

M. Lücke
Fachrichtung Theoretische Physik, Universität des Saarlandes, D-6600 Saarbrücken, West Germany and Institut für Festkörperforschung der Kernforschungsanlage Jülich, D-5170 Jülich, West Germany*

M. Mihelcic and K. Wingerath
Institut für Festkörperforschung der Kernforschungsanlage Jülich, D-5170 Jülich, West Germany
(Received 10 April 1984)

We present numerical solutions of the Navier-Stokes equations for the time evolution of axisymmetric flows between concentric cylinders of three different radius ratios η in the range $0.5<\eta<0.9$ after the Reynolds number R is suddenly increased from a subcritical to a supercritical value in the range of $\epsilon=R/R_c-1$ between 0.01 and 0.1. Such a procedure generates a propagating interface between the stable Taylor vortex state that grows first near a rigid nonrotating end plate and the unstable homogeneous circular Couette flow which is formed in the bulk of the annulus very shortly after increasing the driving. Step up from stationary flow states at finite subcritical driving and sudden starts from rest are simulated. We determine for both cases the behavior of the Ekman vortex system near an annulus end. The time evolution of the unstable circular Couette flow in the bulk is found to agree perfectly with the analytical solution for an infinite annulus. We discuss the effect of inhomogeneities that break the translational symmetry in axial direction, thereby generate local vortex flow, and thus compete against front propagation in the destruction of the homogeneous flow state. The evolution of the intensity and the structure of the vortex pattern behind the moving interface and various other properties of the fronts are determined in quantitative detail and compared with theoretical and experimental results. The axial intensity profiles of the Taylor vortex fronts are about 20% sharper than those we have derived from the lowest-order amplitude equation. In agreement with the latter, the front extension suitably defined varies as $\sim\epsilon^{-1/2}$ and the propagation velocity varies as $\sim\epsilon^{1/2}$ in the driving range considered here.

I. INTRODUCTION

Many dissipative systems undergo, at a critical value of the driving, a transition from a stationary spatially homogeneous state that is subcritically stable to a spatially periodic state that is supercritically stable. Examples are the Couette-Taylor system,[1] Rayleigh-Bénard convection,[2], crystal growth,[3] chemical reactions,[4] etc. The mechanisms involved in the pattern formation and wave-number selection are very complex and poorly understood. For example, the equations of motion for the above hydrodynamic systems have a continuum of linearly stable solutions with different wave numbers in the case of an infinite spatial extension.[5,6] In finite systems, however, boundary conditions and the history of the driving up to the final supercritical value seem to select one of a finite number of periodic patterns. Then, however, this dissipative structure—for example, the Taylor vortex flow (TVF) in the Couette-Taylor system—can be compressed or dilated continuously within a band of wavelengths by moving one of the two rigid horizontal boundaries at the ends of the annulus.[7] On the other hand, if the pinning of the periodic pattern is eliminated[8] or at least considerably reduced at one end, as done in the experiments of Cannell *et al.*,[9] then always a unique wavelength seems to be realized.[9,10]

In this work we shall investigate a pattern-formation problem which has attracted much research activity lately: the growth of the periodic structure behind an interface which spatially separates, at supercritical driving, the periodic state from the unstable homogeneous state, with the interface moving into the spatial region occupied by the latter. In many cases, such as, e.g., solidification[11] or flame-front propagation,[12] the evolution of the interface being, itself, subject to various instabilities is so complicated that it is questionable whether the model equations studied so far are appropriate. On the other hand, for the Couette-Taylor problem the equations describing the fluid flow, i.e., the Navier-Stokes equations (NSE's), are well known. They are numerically tractable and amenable to analytical studies. Realistic, yet sufficiently simple approximations are available. Last, but not least, with a reasonable amount of care to avoid imperfections of the concentric cylinders, it is experimentally very easy to generate and to observe[13] the pattern formation of periodic TVF that grows into the homogeneous circular Couette flow (CCF) and thereby generates a moving front. For various reasons it seems to be considerably more difficult to perform an analogous experiment for propagating Rayleigh-Bénard convection. We thus deem the Couette-Taylor system well suited for a *detailed, quantitative* study of problems related to interfacial pattern formation in a real system.

A propagating interface between the axially periodic

TVF state and the axially homogeneous CCF state can be generated—in experiments as well as in numerical simulations—by a sudden step up of the driving from a subcritical to a supercritical value. Thereafter, vortices start growing first near an end of the annulus—be it a rigid nonrotating plate bounding the fluid,[13,14] a plate rotating with the inner cylinder,[15] or a free-slip boundary[13,16]—since it is, in general, the largest imperfection breaking the translational symmetry of the system. Then a TVF front is formed, propagating into the bulk of the annulus where the unstable CCF appropriate to the supercritical driving has developed within a very short time after the step up. Note, however, that there is a "nuisance" effect which competes with TVF front propagation to destroy the unstable CCF, that is, nucleation of TVF from ever-present imperfections that break the translational symmetry in the axial direction and thereby induce radial and axial flow. Thus the "simple" procedure for observing TVF fronts is to make the inhomogeneities so small that the time for nucleation growth is longer than the propagation time in the given annulus (an ideal system in this respect would be one with the only symmetry-breaking imperfection to generate the periodic state being, e.g., an annulus end). Having ensured this, one finds[13,14] TVF intensity fronts propagating into the annulus that are circular symmetric and flat, with the normal of the front plane being parallel to the cylinder axes.

Further details are discussed in this work, which is organized as follows. In Sec. II we describe the system, and in an appendix we give details of our numerical procedure to integrate the NSE's. In Sec. III we compare the analytical solution for the evolution of unstable CCF after a sudden start from rest to a supercritical driving with our numerical result for the flow in the bulk of the annulus. Furthermore, we show in detail how Ekman vortices grow near a rigid nonrotating end plate after a step up. Section IV contains our results on propagating TVF fronts and the pattern evolution of the supercritical state behind the front. We make a detailed comparison with predictions of a Ginzburg-Landau–like amplitude equation which describes, to lowest order in an expansion around the critical driving, the evolution of the TVF state. Section V contains a summary.

II. THE SYSTEM

We have investigated time-dependent, rotationally symmetric flows of a viscous, incompressible fluid between concentric cylinders. The outer one (radius r_2) was always at rest and the inner one (radius r_1) was rotating. We used setups with three different radius ratios, $\eta=r_1/r_2=0.5066$, 0.75, and 0.893. The last one was chosen for comparison[14] with front-propagation experiments of Ahlers and Cannell,[13] and $\eta=0.5066$ was chosen to check TVF amplitudes against laser Doppler velocimetry measurements of Pfister and Rehberg.[17] In all cases, Γ, the aspect ratio of cylinder length to gap width $d=r_2-r_1$, was 25. In addition, we made one control run for a longer annulus, $\Gamma=50$, of radius ratio $\eta=0.893$.

The evolution of such flows is described by the momentum-balance equations for the velocity field $\vec{u}$, i.e., the Navier-Stokes equations,

$$(\partial_t+\vec{u}\cdot\vec{\nabla})\vec{u}=-\frac{1}{\rho}\vec{\nabla}p+\nu\nabla^2\vec{u}\ . \tag{2.1a}$$

Here, ν denotes the kinematic viscosity. The pressure field p is related to the velocity field $\vec{u}$ via a Poisson equation, cf. Appendix. The continuity equation for the constant mass density ρ,

$$\vec{\nabla}\cdot\vec{u}=0\ , \tag{2.1b}$$

implies that the field $\vec{u}$ is solenoidal. It is convenient to decompose the velocity

$$\vec{u}=u\vec{e}_r+v\vec{e}_\phi+w\vec{e}_z \tag{2.2}$$

in a cylindrical coordinate system into a radial part u, an azimuthal component v, and an axial velocity w, as shown in Fig. 1. They all depend on r, z, and t, but not on ϕ. When presenting our results we shall measure distances in units of the gap width d, and times in units of the characteristic time

$$\tau=d^2/2\pi\nu \tag{2.3}$$

for diffusing azimuthal momentum across the gap.

In the Appendix we discuss the numerical procedure to solve the NSE (2.1). All solutions were obtained subject to the condition that the velocity field is specified on all boundaries of the annulus. For example, $\vec{u}=0$ at the surface, $r=r_2$, of the outer cylinder, and at the solid stationary top plate, $z=\Gamma d$, bounding the fluid, and $\vec{u}=v_1\vec{e}_\phi$ on the surface, $r=r_1$, of a rigid inner cylinder rotating with angular velocity v_1/r_1. Other boundary conditions are discussed in Sec. III B.

The basic state for small driving, i.e., small rotation speed v_1 of the inner cylinder, is circular Couette flow. This flow is stationary and homogeneous in the z direction. It has no radial and axial components,

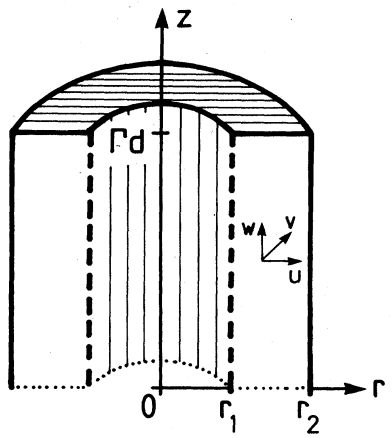

FIG. 1. Axial cross section (not to scale) of the concentric cylinders. Horizontally hatched area denotes a rigid nonrotating plate in contact with the fluid. Taylor vortex flow fronts propagate downwards from the rigid plate into the bulk of the annulus (white area). Axes labeled u, v, and w indicate the decomposition (2.2) of the velocity field.

$$u=w=0\ ,\quad v_{\mathrm{CCF}}(r)=v_1\left[\frac{r_2}{r}-\frac{r}{r_2}\right]\frac{\eta}{1-\eta^2}\ . \tag{2.4}$$

The tangential velocity $v_{\mathrm{CCF}}(r)$ drops monotonously from v_1 at r_1 to zero at r_2. This flow is realized in the bulk of annuli sufficiently far away from top and bottom ends if the Reynolds number,

$$R=v_1 d/\nu\ , \tag{2.5}$$

is below the critical one, $R_c(\eta)$,[1] for the onset of Taylor vortex flow in an idealized system consisting of infinitely long cylinders. However, CCF is not realizable close to physical horizontal boundaries that break the translational invariance of (2.4). Rigid stationary plates, e.g., enforce the fluid velocity to drop to zero, and, more importantly, thereby induce, for all Reynolds numbers, vortex flow in their vicinity.[18] The intensity of such an Ekman vortex system[17] rapidly falls off towards the bulk of the annulus if the driving is sufficiently subcritical (cf. Sec. III D). The penetration length of the vortex flow into the bulk CCF diverges as R approaches $R_c(\eta)$.[17]

For supercritical driving, i.e., for positive

$$\epsilon=R/R_c(\eta)-1\ , \tag{2.6}$$

small deviations from CCF grow as a result of unbalanced centrifugal forces. Thus, in the presence of perturbations, the homogeneous CCF state decays into another stationary state, TVF, which is spatially periodic in the z direction. Therein, a vertical stack of toroidal vortices, wrapped around the inner cylinder, is formed with alternating flow directions in the r-z plane. Again, this stationary TVF state is periodic only away from horizontal boundaries. The vertical extension of a vortex pair, i.e., the periodicity length λ of the TVF state is about $2d$.

In the next section we describe how to generate, at supercritical driving, a flow such that a limited region near the top plate is occupied by the stable TVF state, while the rest of the annulus is occupied by the unstable CCF state. Then the two flow states are separated by a "domain wall" in a transition region. The profile of this "wall" or front between the stable periodic state and the unstable homogeneous state is determined by the way the TVF intensity falls off towards the bulk CCF.

Given such an initial flow condition, the front itself provides the inhomogeneities, i.e., perturbations of the basic state from which the stable periodic state grows. In this growth process, the TVF intensifies in the transition region. Thus the intensity profile is shifted further downward into the bulk of the annulus, which is still occupied by the unstable CCF. Of course, the latter is true only if the ever-present perturbations of CCF are so small in the bulk that they do not have enough time to grow and thereby destroy the unstable CCF before the TVF front passes by. If that is so, then the TVF state propagates into the CCF state. To be more precise, an intensity profile marking the boundary between the two states propagates into the annulus. The toroidal vortex rings themselves do not move—except for a slow repositioning to adjust wavelengths. It is only the front intensity profile that propagates.

As a representative example for TVF evolution by front propagation from a rigid stationary top plate into the annulus, we show, in Figs. 2(b)–2(f), the radial velocity field in the middle of the gap, $u(r=r_1+d/2,z,t)$, as a function of z at successive equidistant times. Positive (negative) u means radial outflow (inflow). The vertical extension of a particular vortex can be read off from the distance between adjacent outflow and inflow extrema. In Fig. 2(g) we indicate schematically the sixth vortex from the rigid top plate. Figure 2(a) and the boundary condition at the lower end, $z=0$, of the annulus, is discussed in Sec. III B.

To present our results concerning TVF front propagation, it suffices to discuss the radial velocity field, say, in the middle of the gap. The other velocity components and the pressure field are intimately related to the former. For example, the spatial oscillations of the axial velocity $w(z,t)$ are phase-shifted by half a vertical vortex extension, i.e., roughly d, with respect to those of $u(z,t)$. On the other hand, the oscillations of the tangential velocity around the CCF are in phase with those of $u(z,t)$—large v implies radial outflow, while inflow can occur only at

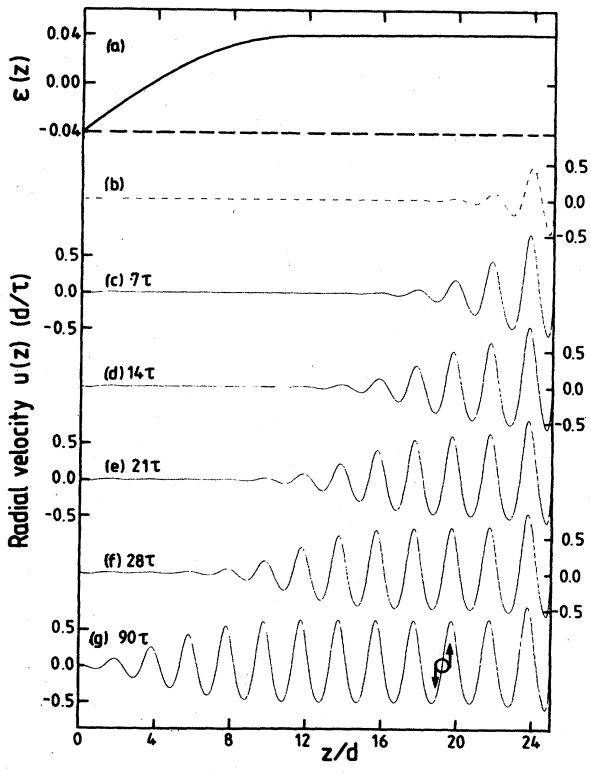

FIG. 2. Time evolution of the radial velocity in the middle of the gap ($\eta=0.893$) after step up to supercritical driving. Radial velocities at different times after the step up are shown in (c)–(g). The initial state is the stationary flow [dashed line in (b)] at subcritical driving [dashed line in (a)]. The top end of the annulus is a nonrotating plate. The subcritical CCF boundary condition at $z=0$ and the spatially ramped driving $\epsilon(z)$ [solid line in (a)] after the step is discussed in Sec. III B. Positions of inflow ($u<0$) and outflow ($u>0$) maxima of the sixth vortex from the top are indicated by arrows in (g) for later reference.

places where the tangential velocity is small. Finally, velocity profiles at other radial positions differ only by their amplitudes, which decrease towards the outer cylinder at rest.

III. GENERATION OF UNSTABLE CCF AND OF A TVF FRONT PROPAGATING INTO IT

Our procedure for generating TVF fronts makes use of the fact that rigid nonrotating plates bounding the fluid at the end of the annulus induce Ekman vortex flow (cf. Sec. III C). The basic procedure is, therefore, to step up the rotation rate of the inner cylinder to a supercritical value where TVF is stable, and let the TVF spread into the bulk of the annulus. There the unstable CCF appropriate to the supercritical driving develops within about 2τ after the driving (cf. Sec. III A). The initial state before the step is either the fluid at rest or a stationary flow at finite subcritical driving (see Sec. III D for a detailed comparison).

A. Evolution of unstable CCF after a step to supercritical driving

In this subsection we show how the unstable CCF state evolves in the bulk of the annulus, i.e., far away from the top plate, shortly after stepping up the rotation rate to a supercritical value. We present results for a sudden start from rest as a representative example.

1. Analytical solution of the NSE

For a sudden start from rest, the flow between ideal infinite cylinders is described—in the absence of imperfections—by

$$u=w=0\ , \tag{3.1a}$$

$$\left[\frac{1}{\nu}\partial_t+\frac{1}{r^2}-\left[\partial_r+\frac{1}{r}\right]\partial_r\right]v(r,t)=0\ , \tag{3.1b}$$

and an equation for the pressure $p(r,t)$ which is determined by the tangential velocity $v(r,t)$. The boundary and initial conditions for this case are

$$v(r_1,t\geq 0)=v_1\ ,\quad v(r_2,t\geq 0)=0\ ,$$
$$v(r_1<r\leq r_2\ ,t=0)=0\ , \tag{3.1c}$$

and $r_1 v_1$ is the rotation rate of the inner cylinder after the start at $t=0$.

Note that, in this procedure, radial and axial flow is generated only in the presence of imperfections that break the translational symmetry in the z direction, e.g., horizontal boundaries, rough cylinder surfaces, or misaligned axes, etc. If they are absent, a start from rest to a supercritical rotation rate does not produce TVF. Of course, in an experimental setup—and also in our numerical code—there are always imperfections. Their size and that of the driving determines how long it takes the radial flow to develop, via local growth, an appreciable intensity. On the other hand, the unstable CCF flow is established on the rather fast time scale of about $(2-3)\tau$, as we will see shortly. Thus, whether and how long one sees unstable supercritical CCF after a start from rest depends, among other things, on the size of the imperfections. From the experimental results of Ahlers and Cannell[13] (Fig. 2), for example, one can estimate that, in the bulk of their annulus, TVF had not grown to an appreciable size prior to roughly 70τ, since at that time they monitored the arrival of a TVF front.

The solution of (3.1) may be obtained[19] by Hankel transforms.[20] We shall decompose it according to

$$v(r,t)=v_{\mathrm{CCF}}(r)+\tilde{v}(r,t) \tag{3.2a}$$

into the stationary final Couette velocity profile $v_{\mathrm{CCF}}(r)$, (2.4), and into the transient part

$$\tilde{v}(r,t)=v_1\pi\sum_{n=1}^{\infty}\frac{J_1[x_n(r/r_1)]Y_1(x_n)-J_1(x_n)Y_1[x_n(r/r_1)]}{J_1^2(x_n)/J_1^2(x_n/\eta)-1}e^{-x_n^2 t\nu/r_1^2}\ . \tag{3.2b}$$

Here, J_1 and Y_1 are Bessel functions and the x_n's are roots of the equation

$$J_1(x/\eta)Y_1(x)=J_1(x)Y_1(x/\eta)\ . \tag{3.3}$$

We determined up to 380 roots for reasons explained further below.

2. Comparison with numerical simulation

In Fig. 3 we show the radial buildup of the tangential velocity after a sudden start from rest towards the CCF profile. Solid lines represent the analytical solutions $v(r,t)$, (3.2), at times 0.118τ, 0.236τ, 0.472τ, 0.943τ, and 4.72τ, respectively, after the step up. The velocity profile at the latest time shown is practically indistinguishable from the CCF solution. Dots denote the tangential velocity $v(r,z=14d,t)$ obtained in the full numerical simulation (cf. Appendix) of the NSE (2.1) for our finite system at the axial position $z=14d$, i.e., $11d$ below the rigid top plate. Obviously the agreement is perfect. Note that the TVF front propagating downwards from the rigid top plate arrives, in our example, at $z=14d$ only after about 20τ.

In Fig. 4 we show the time dependence of the growth of the tangential velocity in the middle of the gap in the time interval covered by Fig. 3. Again, the solid line is the analytical result and the dots denote the tangential velocity $v(r=r_1+d/2, z=14d, t)$ obtained in our simulation.

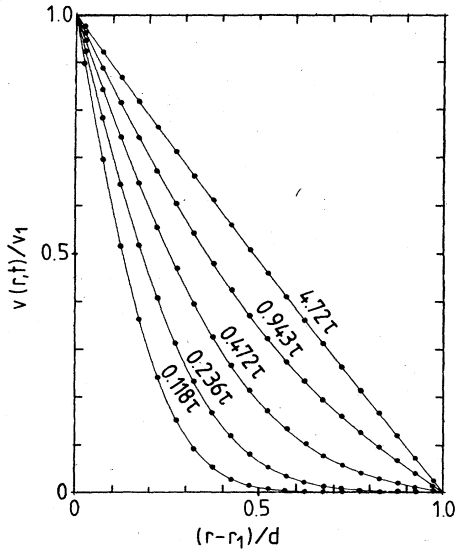

FIG. 3. Time evolution of the tangential velocity towards the CCF profile after a sudden start from rest to supercritical driving $\epsilon_0=0.04$ ($\eta=0.893$). Lines represent the analytical solution (3.2) of the NSE for an infinite ideal system. Dots show the tangential velocities $v(r,z=14d,t)/v_1$ obtained in the numerical simulation of our finite system. The profile at the latest time shown is practically indistinguishable from the CCF solution (2.4).

Here, the agreement is also perfect down to times of about 0.1τ. For such small times after the sudden start, there arise technical problems with the analytical solution (3.2) and (3.3): Truncating the infinite sum (3.2b) at too low an order causes unphysical oscillations of $\tilde{v}(r,t)$ at small times. Our 380 roots ensured their amplitudes to be less than about 10^{-3} in Fig. 4.

Note that at time 2τ the tangential velocity in the middle of the gap has already reached 95% of the CCF value. This figure, together with Fig. 3, makes it clear that the characteristic time for diffusing azimuthal momentum tranversally across the gap d is $\tau=d^2/2\pi\nu$ and not d^2/ν.

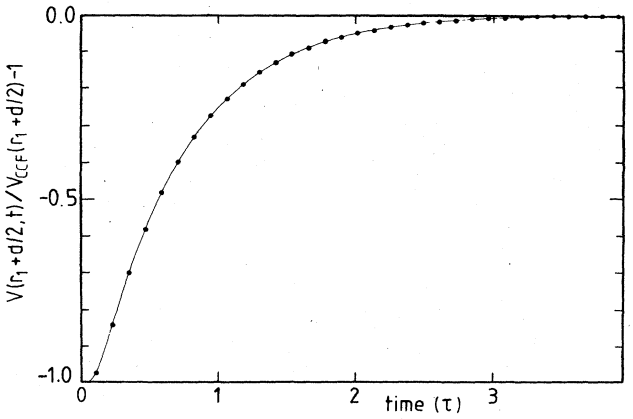

FIG. 4. Time evolution of tangential velocity in the middle of the gap ($\eta=0.893$) at $r=r_1+d/2$ after start from rest to supercritical driving $\epsilon_0=0.04$. Solid line denotes the analytical result and dots represent the velocity obtained in our simulation at the axial position $z=14d$.

B. Suppression of TVF at the lower end of the annulus

To maximize the time and length over which we could monitor front propagation in our modestly long annuli, we generated a single front propagating downwards from the rigid nonrotating top plate at $z=25d$. A possible second front that might propagate upwards into the annulus from the bottom horizontal boundary was suppressed by imposing CCF boundary conditions at $z=0$, with a subcritical tangential velocity, $v_1(z=0)/v_1^c=1-\epsilon_0$, at the inner cylinder that damps out vortex flow. In particular, the stationary flow resulting from spatially constant subcritical driving, $v_1(z)/v_1^c=1-\epsilon_0$, does not have any Ekman vortices at the lower end of the annulus—$u=0$ close to $z=0$—while the rigid top plate causes vortex flow. See, e.g., the stationary radial velocity field in Fig. 2(b) resulting from the constant subcritical driving $\epsilon(z)=-0.04$ as a representative example.

In our computation we stepped up the tangential boundary condition at the inner cylinder to the driving profile [solid line in Fig. 2(a)],

$$\frac{v_1(z)}{v_1^c}-1=\epsilon(z)=\epsilon_0\times\begin{cases}1-2(1-z/12d)^2 & \text{for } z<12d\\ 1 & \text{for } z\geq 12d\end{cases}, \tag{3.4}$$

consisting of a supercritical plateau and a parabolic ramp decreasing smoothly to the subcritical value $\epsilon(z=0)=-\epsilon_0$. The suppression of radial flow at the lower end of the annulus in this procedure is not complete, despite the subcritical CCF boundary condition at $z=0$, since the step up causes impulsive axial shear which induces weak vortex flow. Detailed investigation shows that the perturbation moves upwards into the annulus, as is barely visible in Figs. 2(c)–2(f). However, being located initially in the region with subcritical driving, $\epsilon(z)<0$, its growth is sufficiently impeded as not to disturb the main front propagating downwards in Figs. 2(c)–2(f). Vortex flow is induced also near $z=12d$, where the parabolic ramp $\epsilon(z)$, (3.4), merges with the supercritical-driving plateau, the perturbation of the basic circular flow, however, being extremely weak there. (We note parenthetically that it is more pronounced for a linearly ramped Reynolds number joining, with a discontinuous derivative, to the supercritical plateau.)

Here, however, the main TVF front propagating downwards from the top plate into the region with constant supercritical driving is not disturbed: In the driving range $\epsilon_0<0.1$ explored in this work ($\epsilon_0=0.1$ already being a borderline case), the perturbations did not have enough time to grow to a dangerous size in that region, $z>12d$, where front properties were determined.

In our control run for the longer annulus, $\Gamma=50$, with the same driving ramp $\epsilon(z)$, (3.4), and $\epsilon_0=0.04$, with the propagation path and time being longer, the above perturbations of the circular flow have enough time to grow to sizable TVF intensities before the main front propagating downwards from $z=50d$ reaches $12d$. In fact, they generate a second, upward-moving TVF front[16] which col-

lides with the main one near $z=24d$.

Generation of Ekman vortices can also be avoided by enforcing mirror symmetry at $z=0$ with spatially constant driving.[15] This has advantages in a study of front propagation. Since we have also been interested in wave-number and pattern selection (in systems with spatially ramped driving), we preferred our procedure.

C. Growth of Ekman vortices

Here we investigate the time evolution of Ekman vortices, i.e., vortices nearest to the rigid upper plate, after stepping up the inner cylinder's rotation rate. We discuss a start from rest to a supercritical driving rate. Step up from a subcritical stationary flow state entails similar growth behavior of Ekman vortices.

In Fig. 5(a) we show the radial velocity in the middle of the gap as a function of distance from the top plate at seven successive times t_n increasing with the power law $t_n/\tau=0.116\times 2^n$ in the interval $0.116\leq t/\tau\leq 7.4$ after a sudden start from rest to $\epsilon_0=0.04$. In Figs. 5(b) and 5(c) we show the time evolution of the radial velocity in the middle of the gap at the axial position indicated by arrows b and c in Fig. 5(a), i.e., the final location of the first outflow and inflow maxima. These velocities reach 90% of their final value at times $\simeq 5\tau$ and $\simeq 2.3\tau$, respectively, after the sudden start, as can be seen in Figs. 5(b) and 5(c). During this time, the unstable CCF appropriate to the subcritical driving has already fully developed in the bulk of the annulus (cf. Sec. III A). The Ekman-vortex system, on the other hand, is then still well localized in the immediate vicinity of the top plate, according to Fig. 6. Therein, we show intensity maxima of radial inflow and outflow in the middle of the gap as a function of distance from the top plate at time 4.62τ after a sudden start to two different supercritical rotation rates. Note the logarithmic scale: At a distance of, e.g., $5d$, the radial flow intensity is, at the above time, still about 3 orders of magnitude smaller than that near the plate.

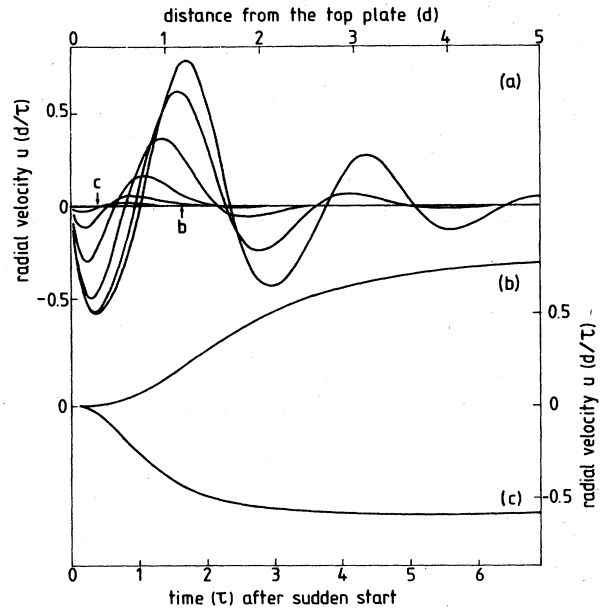

FIG. 5. Growth of Ekman vortices after sudden start from rest to supercritical rotation rate $\epsilon_0=0.04$. Curves in (a) show radial velocities in the middle of the gap ($\eta=0.893$) vs distance from the rigid top plate at seven successive times $0.116\times 2^n\tau$ ($n=0,1,\ldots,6$). Curves in (b) and (c) represent the radial outflow and inflow velocities at positions marked by arrows b and c, respectively, in (a) as functions of time.

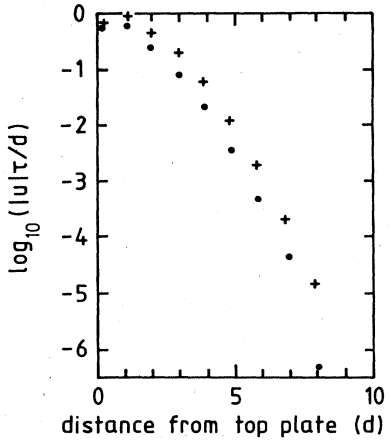

FIG. 6. Vortex intensities shortly after sudden start from rest. Dots (crosses) denote radial inflow and outflow maxima in the middle of the gap of cylinders with radius ratio $\eta=0.893$ at time 4.62τ after step up to $\epsilon_0=0.02$ (0.08).

D. Start from rest and step up from stationary subcritical flow state

Figures 3–6 demonstrate that, at about 5τ after a sudden start from rest to supercritical driving, we have generated (i) the unstable CCF state in the bulk of the annulus, and (ii) a TVF "perturbation" that is well localized near the rigid upper plate. So good an initial localization of the TVF state cannot be achieved by the alternative procedure originally employed by Ahlers and Cannell:[13]

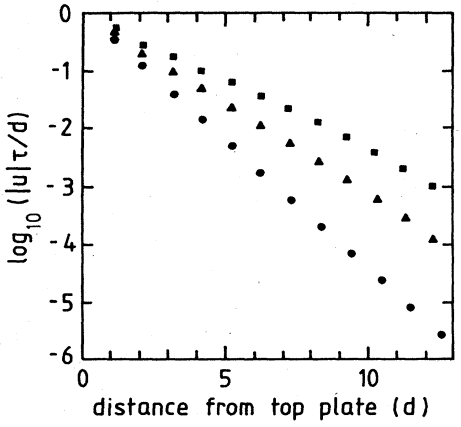

FIG. 7. Intensity profiles of stationary, subcritical Ekman-vortex systems. Symbols denote successive radial inflow and outflow maxima in the middle of the gap of cylinders with radius ratios $\eta=0.893$ for $\epsilon=-0.08$ (dots), -0.04 (triangles), and -0.02 (squares).

If the state before the step up is a slightly subcritical stationary flow, the subcritical Ekman-vortex system established prior to the step reaches far into the annulus. This is documented in Fig. 7 for three different subcritical rotation rates. As a small digression, we note that a fit of the profiles of Fig. 7 to an exponential yields an Ekman-vortex penetration depth δ into the bulk varying roughly as

$$\delta \simeq 0.65 \,|\epsilon|^{-1/2} d \tag{3.5}$$

in the considered driving range.

In Fig. 8 we compare the extension of the vortex intensity profile into the unstable CCF state after a start from rest to $\epsilon_0=0.04$ (dots) with that (squares) after a step up to the same driving, however, from the stationary subcritical state at $\epsilon=-0.04$. In each case, 4.62τ has elapsed since the step up. For later reference, we have also included, denoted by crosses, the stationary intensity profile of the initial subcritical Ekman-vortex system. Figure 8 clearly shows that, in an annulus of given length, a sudden start from rest has the technical advantage of allowing exploitation of a longer propagation path than that allowed by a step up from a stationary subcritical state with an extended Ekman-vortex system.

E. Nucleation versus front propagation

Consider the TVF evolution shortly after a step up from a stationary subcritical flow as documented, e.g., in Fig. 8: Within the time 4.62τ, the vortex intensity has grown from the profile before the step up shown by crosses to that marked by squares. This growth is not a nucleation process, but rather is caused by TVF front propagation. The former process would produce, according to the amplitude equation (cf. Sec. IV A) within the time $\Delta t=4.62\tau$, an enhancement of a small homogeneous perturbation by only a factor of about $\exp(\epsilon_0 \Delta t/\tau_0)=2.17$

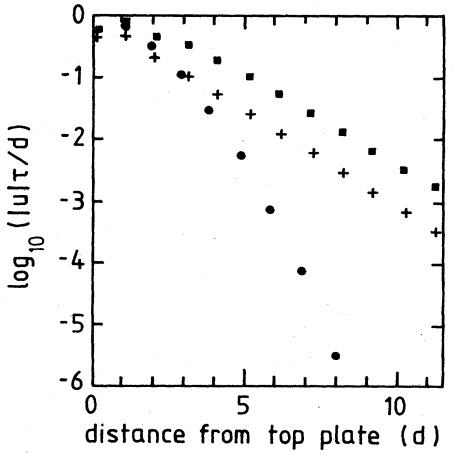

FIG. 8. Intensity profile of vortex flow shortly after different steps to supercritical driving $\epsilon_0=0.4$. Dots and squares denote maxima of the radial velocity in the middle of the gap ($\eta=0.893$) at time 4.62τ after step up from rest and from stationary subcritical state at $\epsilon=-0.04$, respectively. Crosses denote intensity profile of that stationary subcritical state.

in the case of Fig. 8. Here, however, the local enhancement of vortex intensities, i.e., the *vertical* distance between crosses and squares in Fig. 8, is about 3 times larger. Instead, one must interpret the evolution of the intensity profile (crosses to squares) in terms of a *horizontal* displacement, i.e., a spatial translation of the intensity profile: The *horizontal* distance between crosses and squares is about the distance that a fully developed TVF front travels within the above time interval.[14] Note, however, that the distinction between TVF front propagation and nucleation becomes less and less clear cut the further an initially present subcritical vortex flow extends into the annulus, i.e., the smaller ϵ_0 is. A detailed investigation of front propagation in our annuli, and a discussion of nucleation and front propagation within the framework of the amplitude equation, is presented in Sec. IV A.

IV. PROPAGATING TVF FRONTS

In this section we present our results on propagating TVF fronts and compare them with predictions of the lowest-order amplitude equation.

A. Lowest-order amplitude equation

To lowest order in $(|\epsilon|)^{1/2}$, (2.6), of an expansion[21] of the NSE, the radial velocity field in an infinite cylinder evolves according to

$$u(r,z,t)=\mathrm{Re}[A(z,t)e^{ik_c z}u_{\mathrm{lin}}(r)] \,. \tag{4.1}$$

Here, $u_{\mathrm{lin}}(r)$ is determined in a linear stability analysis by the mode with axial wave number $k_c \simeq \pi/d$ that first grows at $R_c(\eta)$. Normalizing $u_{\mathrm{lin}}(r)$ to unity in the middle of the gap, the amplitude of axial oscillations of the radial velocity, $u(r_1+d/2)$, z, t), is given by $|A(z,t)|$. For $(|\epsilon|)^{1/2} \ll 1$ this amplitude of the "order parameter" u is a slowly varying function of z and t determined by the solution of the Ginzburg-Landau equation,

$$\tau_0 \partial_t A=(\xi_0^2 \partial_z^2+\epsilon-g\,|A\,|^2)A \,. \tag{4.2}$$

The coupling constant g follows from a lowest-order nonlinear analysis.[22] The length scale ξ_0 is determined by the curvature of the stability boundary of the CCF state at R_c, and τ_0 is determined by the growth rate of the critical mode k_c. Both quantities may be obtained from a linear stability analysis. One finds[23] that they are very weakly dependent on the radius ratio η. In the range $0.5<\eta<0.9$ explored in this work, ξ_0 varies between $0.276d$ and $0.27d$, and τ_0 varies between 0.234τ and 0.24τ, so that the velocity ξ_0/τ_0 is constant within 1.1%. Note that the quantities in Ref. 23 are defined with respect to Taylor numbers, $T/T_c-1=2\epsilon(1+\epsilon/2)$. The correspondence is $\sqrt{2}\xi_0=\xi_0$ (Ref. 23) and $\tau_0^{-1}=2\sigma_0$ (Ref. 23).

Equation (4.2) determines, to lowest order in $\sqrt{\epsilon}$, the time evolution of an initial disturbance $A(z,t=0)$ of the CCF towards the fully developed periodic TVF state with a homogeneous amplitude given by

$$|A_\infty^2|=\epsilon/g \,. \tag{4.3}$$

For the general growth behavior, there are no closed

analytical formulas. However, two important special cases we are interested in are amenable to analytical studies: (i) homogeneous nucleation and (ii) front propagation. The first describes growth of a *homogeneous* initial amplitude $A(t=0)$ towards A_∞ according to the well-known solution,

$$\left|\frac{A(t)}{A(t=0)}\right| = e^{\epsilon t/\tau_0}\left[1-\left|\frac{A(t=0)}{A_\infty}\right|^2(1-e^{2\epsilon t/\tau_0})\right]^{-1/2}, \tag{4.4}$$

of Eq. (4.2). Note that here the initial amplification rate of a perturbation is ϵ/τ_0.

The other growth mode, case (ii), of the TVF state is determined by a real solution,

$$f(x)=A(z,t)/A_\infty\ ,\quad x=\sqrt{\epsilon}z/\xi_0-\tilde{c}\epsilon t/\tau_0\ , \tag{4.5}$$

of Eq. (4.2). It describes a disturbance of the CCF state propagating with arbitrary, i.e., so far undetermined, reduced velocity, $\tilde{c}>0$. In unreduced units the velocity is

$$c_A=\tilde{c}\sqrt{\epsilon}\xi_0/\tau_0\ . \tag{4.6}$$

Every intensity profile $f(x)$ of such a propagating amplitude distribution is (mathematically) possible that solves the equation

$$\left[\frac{d^2}{dx^2}+\tilde{c}\frac{d}{dx}\right]f(x)=-\frac{\partial V(f)}{\partial f}\ , \tag{4.7a}$$

which follows from inserting (4.5) into (4.2), and

$$V(f)=\tfrac{1}{2}f^2-\tfrac{1}{4}f^4\ . \tag{4.7b}$$

Of course, the boundary conditions imposed on f make the solution unique. We are interested in TVF fronts for which $f(x\to\infty)=0$ and $f(x\to-\infty)=1$. The former (latter) corresponds to the CCF (TVF) state in the distant past (future) or at large positive (negative) z.

It is helpful to interpret[24] $f(x)$ as the position at "time" x of a particle in the inverted double-well potential $V(f)$, (4.7b). This particle starts rolling downwards from the maximum at $f=1$ at "time" $x=-\infty$, and ends up in the minimum at $f=0$ at "time" $x=+\infty$ as a result of the finite "friction" $\tilde{c}>0$. Linearization around $f=0$ shows that the characteristic exponents are complex conjugate (real, negative) if $\tilde{c}$ is less (greater) than 2. The aperiodic-limit case $\tilde{c}=2$ marks the boundary between the oscillatory and monotonous approach of $f(x\to\infty)$ towards zero.

Aronson and Weinberger[25] have shown that a very wide class of initial amplitude distributions $0\le A(z)/A_\infty\le 1$, in particular, all those that are localized in a finite-z region, evolve into a TVF front between the CCF state $f=0$ and the TVF state $f=1$ that propagates with the borderline velocity $\tilde{c}=2$. Given this quite remarkable result, we shall henceforth discuss only this final, universal front solution of (4.2).

Since we are not aware of an analytical expression for the unique front intensity profile $f(x)$ for $\tilde{c}=2$, we integrate (4.7) numerically. The result shown in Fig. 9 has, to our knowledge, not been published so far. Starting values were $f=1-10^{-4}$ and $f'=-(\sqrt{3}-1)\times 10^{-4}$, with the latter following from linearization around $f=1$. To measure the front extension we determined the distance $\tilde{l}$, over which the intensity increases from $\frac{1}{4}$ to $\frac{3}{4}$ as $\tilde{l}=2.941$. This means that, in unreduced units, the so-defined front extension

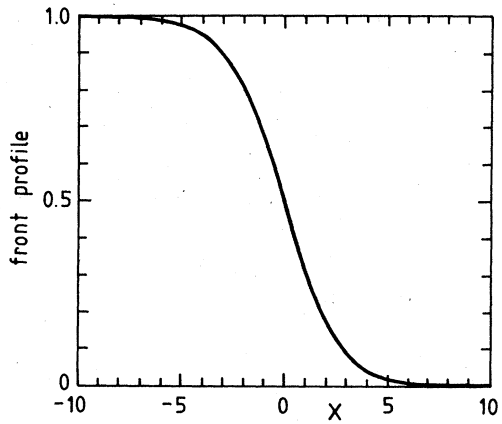

FIG. 9. Intensity profile $f(x)$ of the front following from the amplitude equation (4.7) for the reduced velocity $\tilde{c}=2$. The front extension defined as the reduced length over which the intensity increases from 0.25 to 0.75 is $\tilde{l}=2.94$.

$$l_A=2.941\epsilon^{-1/2}\xi_0 \tag{4.8}$$

is predicted by the amplitude equation to diverge as $\sim\epsilon^{-1/2}$ for $\epsilon\to 0$.

Finally, we compare the growth of a small perturbation of the CCF state via homogeneous nucleation (4.4) with that one caused by a TVF front passing a fixed observation point. Let this point be in the head of the front where $f(x)\ll 1$. There the local amplitude grows by the factor

$$e^{2\epsilon\Delta t/\tau_0}\left[1-2\epsilon\frac{\Delta t}{\tau_0}\left[1+\frac{f'(x)}{f(x)}\right]\right] \tag{4.9}$$

within the time Δt. This result follows from linearizing (4.7) around $f=0$. Thus the local growth rate of the TVF amplitude in the head of the front is about twice as large as the rate in homogeneous nucleation (4.4). This is an "inertia" effect. For homogeneous nucleation the second-order derivative term in (4.2) and (4.7) vanishes. In such an overdamped situation the "particle" takes longer "time" to cover a given "distance" Δf near the minimum of the potential (4.7b). A nonvanishing term $\xi_0^2\partial_z^2 A(z,t)$ causes growth enhancement.

B. Developed TVF

Since many of our data for propagating fronts are most conveniently expressed in relation to the fully developed TVF state, we first discuss those results for the latter case that we need later on. In order to give an impression as to how the fully developed periodic TVF state looks in the bulk of the annulus, we included in Fig. 2(g) the radial velocity field in the middle of the gap long after the step to supercritical driving, $\epsilon_0=0.04$. As a reference for the

fully developed bulk TVF state, we shall henceforth use the velocity field of the sixth vortex from the top rigid plate [as indicated schematically by a small circle in Fig. 2(g)] at the end of our numerical integrations. The times in question—about 30τ (100τ) for our largest (smallest) driving—were sufficiently long to let the front propagate along the full length of our annulus, i.e., to be far away from the vortex in question, and, secondly, to ensure that the *amplitude* of this vortex is stationary (cf. our discussion at the end of this subsection) roughly on a percent level.

1. Flow intensities

Figure 10 shows the radial outflow velocity u_{out} (solid symbols) and the radial inflow velocity u_{in} (open symbols) of this reference vortex, in the middle of the gap, as a function of driving ϵ_0. Also included are fits of Gollub and Freilich[26] to bulk outflow (thick-dashed line) and inflow (thin-dashed line) maxima obtained for a radius ratio $\eta=0.61$, together with their typical error bars. The result of the lowest-order amplitude equation[22] for the radial amplitude in the middle of the gap of an infinite cylinder of radius ratio $\eta=0.5$ is indicated by an arrow. This value has also been deduced by Pfister and Rehberg[17] from a theoretical fit to their outflow maxima measured as a function of distance from rigid end plates.

The amplitudes vary roughly proportionally to $(\epsilon_0)^{1/2}$. Our values, say, for the averaged radial intensity $(u_{in}+u_{out})/2$ of the reference vortex, are larger than the result of the amplitude equation and, moreover, they deviate for *smaller* driving from the $(\epsilon_0)^{1/2}$ behavior. This is a proximity effect of the Ekman vortices near the rigid plate: They are more intensive than the bulk vortices and, in addition, the length over which the intensity of the Ekman-vortex systems falls to the bulk TVF value increases with decreasing $\epsilon_0 \to 0$.[17] Gollub and Freilich[26] found, in the spatial analysis of their radial velocity field, a second harmonic, $A_2\cos(2kz)$, with an amplitude $A_2 \sim \epsilon^{0.79\pm0.03}$. This is in disagreement with an amplitude expansion which yields $A_2 \sim \epsilon$. If one would replace, in an *ad hoc* fashion, their exponent 0.79 by 1, then the thick- (thin-) dashed line in Fig. 10 would be shifted downwards by 6—7 % (upwards by 8—10 %).

The solid symbols in Fig. 11(a) show the ratio u_{in}/u_{out} of radial inflow and outflow velocities of the reference vortex as a function of driving. The dashed curve with the error bar represents the result of Gollub and Freilich[26] (the above-described replacement of the exponent would shift the dashed curve upwards to about 0.92 at $\epsilon=0.01$ and to 0.76 at $\epsilon=0.1$). The arrow indicates that the radial velocity field obtained from the lowest-order amplitude equation varies as $\sim\cos(kz)$, so that $u_{in}=u_{out}$ in this approximation. The deviation $1-u_{in}/u_{out}$ measures the contributions of higher spatial harmonics, $\sim\cos(nkz)$, to $u(z)$. In an amplitude expansion, they would enter via higher orders in $(\epsilon_0)^{1/2}$. Note that, according to Fig. 11(a), this deviation is already about 20% at $\epsilon_0=0.01$.

2. Spatial structure

With increasing driving, the velocity difference between the fast radial outflow u_{out} and the slow inflow increases, i.e., u_{in}/u_{out} decreases. Simultaneously, the size difference between the axial extensions of radial inflow, Δ_{in}, and of radial outflow, Δ_{out}, grows, so that Δ_{in}/Δ_{out} increases [cf. Fig. 11(b)]. The underlying reason is mass conservation: The transport rates of fast outflow and slow inflow must be the same. Therefore the axial extension Δ_{out} of the former is smaller than Δ_{in}, and, moreover, both vary roughly inversely with the corresponding flow velocities. We defined Δ_{out} (Δ_{in}) by the axial distance between those

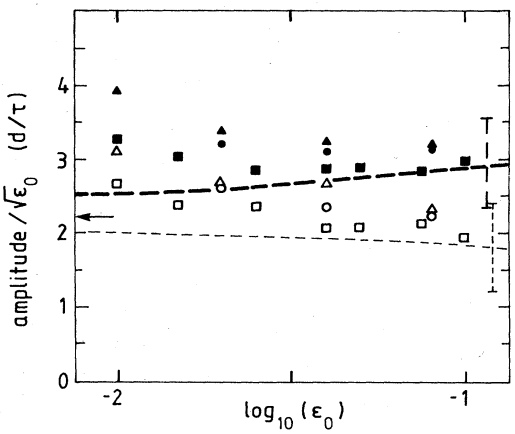

FIG. 10. Amplitudes of radial TVF velocities in the middle of the gap between cylinders of radius ratios $\eta=0.5066$ (squares), $\eta=0.75$ (circles), and $\eta=0.893$ (triangles). Solid (open) symbols denote outflow (inflow) velocities divided by $(\epsilon_0)^{1/2}$ of the sixth vortex [cf. circle in Fig. 2(g)] below the top plate. The arrow indicates the result obtained (Ref. 22) from the lowest-order amplitude equation for $\eta=0.5$. Thick (thin) dashed lines show fits (Ref. 26) to bulk outflow (inflow) maxima for $\eta=0.612$.

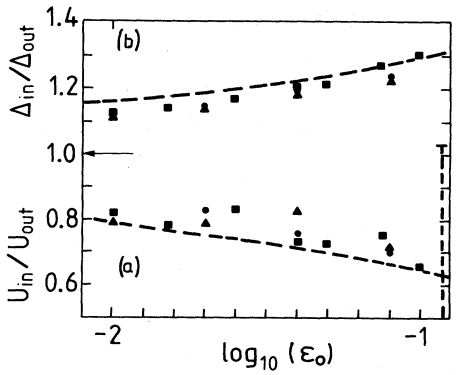

FIG. 11. (a) Ratio of radial inflow and outflow amplitudes of the sixth Taylor vortex below the top plate in the middle of the gap. (b) Ratio Δ_{in}/Δ_{out} of the axial sizes of radial inflow and outflow domains between the sixth vortex and its neighbors. Solid symbols denote our results for radius ratios 0.566 (squares), 0.75 (dots), and 0.893 (triangles). Dashed lines represent the results of Gollub and Freilich (Ref. 26) for a radius ratio $\eta=0.612$. The arrow indicates the prediction of the lowest-order amplitude equation for both (a) and (b).

adjacent nodes of the radial velocity in the middle of the gap, where u is positive (negative) in between. The dashed line in Fig. 11(b) is derived from the representation $A_1\cos(kz)+A_2\cos(2kz)$ used by Gollub and Freilich[26] to fit their data. We determined numerically the zero crossings of the above expression (the exponent replacement $0.79\rightarrow 1$ in A_2 shifts the dashed curve for Δ_{in}/Δ_{out} by about 0.1).

In Fig. 12 we show, for $\eta=0.5066$ as a representative example, how the node distance Δ_{in} (upper dots) increases, and how Δ_{out} (lower dots) decreases, with growing ϵ_0. Triangles denote one-half of the local axial wavelength $\lambda=\Delta_{in}+\Delta_{out}$. For *small* driving, λ seems to approach the wavelength λ_{max}, for which, according to linear stability analysis of the CCF state, a perturbation mode grows fastest. The dashed line represents $\lambda_{max}/2$ obtained by Dominguez-Lerma *et al.*[23] for $\eta=0.5$.

We want to stress that the times at which the data for the bulk reference vortex were taken are too small to let the flow near the top of the cylinder equilibrate via momentum diffusion with that near the bottom end. This would require a time[27] of the order of $\Gamma^2\tau=625\tau$. Thus the above data are not yet fully stationary, say, well below a percent level. In particular, the node distances of the radial velocity have not yet fully equilibrated (the amplitudes are less crucial). This might explain why, at the times at which the data were monitored, the wavelength was still close to λ_{max}, i.e., the local wavelength realized behind a propagating front rather than that of the fully stationary state, which seems to be somewhat larger.[7] We nevertheless found it worthwhile to include Fig. 12, if only to stimulate other research in addition to our own ongoing studies on pattern selection in systems with spatially ramped driving.

Another interesting point we mention, without having an explanation for it, is that the outflow extension Δ_{out} is very close to the small-λ branch of the stability boundary of CCF—crosses in Fig. 12 denote half the axial wavelength at the stability boundary[23] of CCF.

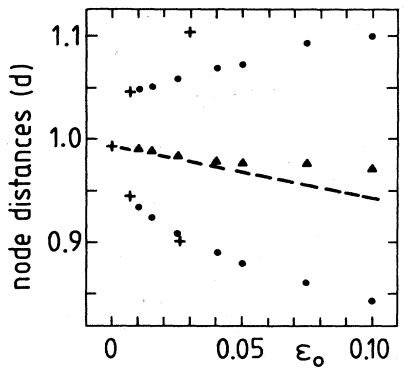

FIG. 12. Axial extension of radial inflow and outflow between the sixth vortex and its neighbors vs driving. Upper (lower) dots denote corresponding node distances Δ_{in} (Δ_{out}) of the radial velocity in the middle of the gap with $\eta=0.5066$. Triangles represent half the axial wavelength $\lambda/2=(\Delta_{in}+\Delta_{out})/2$. Dashed line is half the wavelength with maximal growth rate resulting from a linear analysis (Ref. 23) done for $\eta=0.5$. Crosses show half the wavelengths at the stability boundary (Ref. 23) of CCF for $\eta=0.5$.

C. Propagating TVF fronts

Here we present our numerical results on propagating TVF fronts and compare them with predictions of the amplitude equation (4.2). First, we found[14] that TVF fronts were formed which, after some initial transients, propagated with time-invariant velocity, shape, and intensity profile downwards from the top rigid nonrotating end plate into the bulk of the annulus. We plotted the radial velocity $u(r,z,t)$ at three different radial positions as a function of z and t, and thus found that the three fields always had common axial positions where their intensities increased. Hence the front is a plane and moves at a right angle to the cylinder axes.

1. *Propagation velocity*

In the driving range $0.01\leq\epsilon_0\leq 0.1$, the propagation velocity[14] of our TVF fronts agreed roughly with the universal velocity $\tilde{c}=2$, i.e., $c_A=2(\epsilon_0)^{1/2}\xi_0/\tau_0$ obtained by Aronson and Weinberger[25] for the lowest-order amplitude equation (4.2). The propagation velocities showed practically no variation with the radius ratio η in the range $0.5066\leq\eta\leq 0.893$ covered by our numerical solutions. This is in good agreement with (4.6) since ξ_0/τ_0 is almost independent of η in the above range.

Neitzel[15] found, in a numerical simulation done for $\eta=0.727$ with rotating end plates for $\epsilon_0=0.08$, a front-propagation velocity which agreed very well with the above result. The velocities determined by Ahlers and Cannell from measurements of front arrival times, although showing the $(\epsilon_0)^{1/2}$ variation, were about a factor of 2 smaller than c_A in the above driving range.

2. *Evolution of the TVF pattern*

With respect to the evolution of the periodic pattern under the moving front, we found that the axial size Δ_{in} (Δ_{out}) of a particular radial inflow (outflow) region between two fixed vortices grows (decreases) as the front passes by. Thus, in a frame co-moving with the front, the ratio Δ_{in}/Δ_{out} grows from unity in the extreme precursing head of the front to the bulk value for fully developed TVF discussed in Sec. IV B. This axial variation of Δ_{in} and Δ_{out} seems to be mainly determined by the way the TVF intensity profile of the front grows from zero to the bulk level. Thus the former variation (cf. Fig. 4 in Ref. 14), as a function of the distance behind the front head, is analogous and very similar to the variation of Δ_{in} and Δ_{out} (cf. Fig. 12) for bulk TVF as a function of growing driving ϵ_0. On the other hand, the local wavelengths $\Delta_{in}+\Delta_{out}$ do not vary much under the front. Furthermore, they are close to the one for which a periodic perturbation of the CCF experiences the largest growth rate in a linear stability analysis of the homogeneous flow state.

We want to mention that the mechanism by which the periodic pattern behind the front is determined still puzzles us. Is it the moving interface which selects the pattern behind it (then no slow motion of the nodes should be

expected after the front has passed by), or is the abstract front intensity profile just pushed ahead of the periodic structure, which, originally being determined by the Ekman-vortex system near the annulus end, just expands into the bulk? To answer this question one should prepare spatially localized TVF with different wavelengths as initial states, and see whether, during the expansion of the periodic structure by front propagation, the wavelength of the initial state is kept, in each case, in the bulk sufficiently far behind the front, or whether a different one—possibly a truly unique one—develops.

3. *Intensity profiles of TVF fronts*

In Fig. 13 we show intensity profiles of radial outflow (upper solid curves) and inflow (lower solid curves) maxima in the middle of the gap between cylinders of radius ratio $\eta=0.75$ as a function of distance behind the propagating fronts for three different driving rates. The front profiles of TVF between cylinders of radius ratio $\eta=0.5066$ and 0.893 are similar. The origin of the abscissa in Fig. 13 is chosen to be the position at which the radial flow intensity $|u(z,t)|$ has reached 10% of the outflow velocity u_{out} of bulk TVF as defined in Sec. IV B. We determined, about every 2τ, the size of the radial inflow and outflow maxima and their distance from the moving front position of the 10% intensity level. The thick vertical bars in Fig. 13 reflect the scatter of the so-obtained data. Solid lines are hand-drawn, smooth interpolations.

Note that since outflow away from the rotating cylinder is more intensive than inflow towards it, the radial velocity profiles of Fig. 13 are asymmetric around $u=0$. This asymmetry decreases when the radial flow is very weak, i.e., in the extreme precursing head of the front, and in the limit of small driving $\epsilon_0\to 0$, as discussed in Sec. IV B. Approaching this limit, the front extension grows, cf. curves *a*, *b*, and *c* for $\epsilon_0=0.08$, 0.04, and 0.02, respectively. However, in each case our fronts are sharper than those (dashed curves) following from the amplitude equation (4.2). To obtain the dashed curves, we used the scaling equation (4.5), $A(z)=A_\infty f[(\epsilon_0)^{1/2}z/\xi_0]$, and the universal front profile $f(x)$ of Fig. 9 for the velocity $\tilde{c}=2$. We fixed A_∞ by our bulk intensities, i.e., either $A_\infty=u_{\text{out}}$ or $A_\infty=u_{\text{in}}$. Finally, the resulting intensity profiles $A(z)$ were shifted along the abscissa until they coincided, at the origin of Fig. 13, with the numerical results.

Figure 14 shows the distances l over which our outflow intensities in the front increase from 25% to 75% of the bulk value as a function of driving for our three radius ratios. For better comparison with the prediction, (4.8), of the amplitude equation, $l_A=2.941\epsilon_0^{-1/2}\xi_0$, we have plotted the ratio l/l_A. Thus one infers from Fig. 14 that, in accordance with the prediction of the amplitude equation the front extension defined by l varies roughly proportional to $\epsilon_0^{-1/2}$ in the driving range covered by our calculations. However, real TVF fronts are consistently sharper, by about 20%, in the above driving range. To give an example, for $\eta=0.893$ and $\epsilon_0=0.08$ the front extension l is about $2.3d$, i.e., of the order of the wavelength λ of the TVF state. Since the amplitude equation (4.2) has been derived under the assumption that the TVF intensity distribution $A(z,t)$ is slowly varying on the scale of λ, one cannot expect a realistic description of such a front from it. It is surprising how good the predictions of the amplitude equation are, even in such an extreme situation. For small driving, on the other hand, the square-root increase of $l_A\sim\epsilon_0^{-1/2}$ requires rapidly increasing annuli lengths to

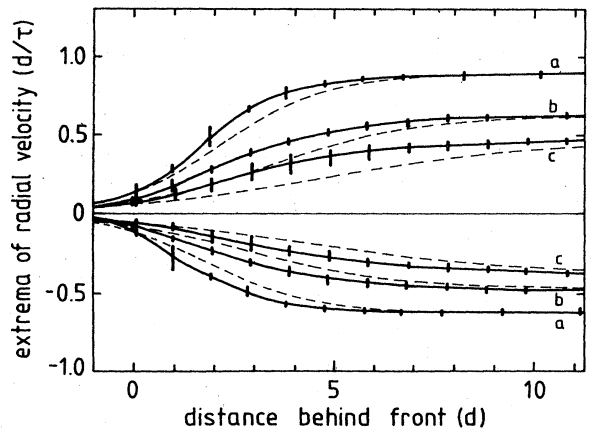

FIG. 13. Intensity profiles of propagating TVF fronts. Upper (lower) solid curves denote smooth interpolations through averaged intensity maxima of radial outflow (inflow) in the moving front in the middle of a gap with $\eta=0.75$ for (a) $\epsilon_0=0.08$, (b) 0.04, and (c) 0.02. The origin of the co-moving frame is the axial position where $|u(z,t)|$ reaches 10% of the bulk outflow velocity u_{out}. Vertical bars indicate the scatter of intensity extrema monitored about every 2τ. Dashed lines are obtained from the universal profile (Fig. 9) resulting from the amplitude equation by normalization to our bulk outflow and inflow intensities u_{out} and u_{in}, respectively. See text for further details.

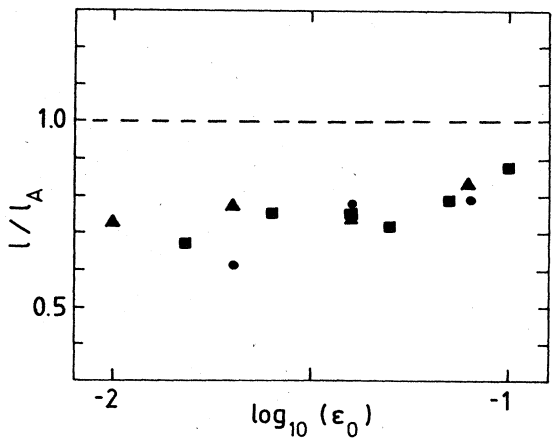

FIG. 14. Extension l of propagating TVF fronts as a function of driving. Here, l is the axial distance over which the radial flow intensity in the middle of the gap rises from 25% to 75% of the bulk TVF value, and $l_A=2.941\xi_0/(\epsilon_0)^{1/2}$ is the prediction of the lowest-order amplitude equation. Symbols denote our results for outflow intensity profiles in annuli of radius ratios $\eta=0.5066$ (squares), 0.75 (dots), and 0.893 (triangles).

provide propagation paths sufficiently long for the moving front to reach stationarity. For example, at $\epsilon_0=0.1$ the steepest part of the front already has an extension l_A of about $8d$.

V. SUMMARY AND CONCLUSIONS

We have solved numerically the time-dependent NSE's for incompressible rotationally symmetric flows between concentric cylinders of three different radius ratios. As in real experiments, propagating TVF fronts were generated by suddenly increasing the rotation rate of the inner cylinder from subcritical values to various Reynolds numbers above the critical one for the onset of TVF. After such a step up—be it from rest or from a stationary subcritical state—the flow evolves as follows.

On the time scale $\tau=d^2/2\pi\nu$, which characterizes transversal transport of azimuthal momentum across the gap, supercritical, unstable CCF is established in the bulk of the annulus, i.e., far away from horizontal boundaries. There, our numerical solution agrees perfectly with the analytical one for sudden start from rest in an ideal, infinitely long system. One could also observe unstable supercritical CCF in real experiments[13] in which the imperfections that destroy the axial homogeneity are so small that the growth time of TVF via nucleation exceeds several τ. A more detailed discussion of the role of imperfections in our system and in a real one is given in Secs. III A and III B.

Within about $(3-4)\tau$, the first two Ekman vortices near a rigid nonrotating end plate, i.e., a no-slip stationary, horizontal boundary at the end of the annulus, have reached their final intensities appropriate to the supercritical driving. For a sudden start from rest, the TVF "disturbance" of the unstable CCF in the bulk is initially—say, after $(3-4)\tau$—much better localized to the vicinity of a rigid plate than for a step up from a stationary subcritical flow state because of the Ekman-vortex system of the latter. However, the final propagation mode of TVF into the CCF state is the same in both cases.

To provide long propagation paths, we generated only one front—at the upper rigid plate bounding the annulus at $z=25d$. The other front was suppressed, to a large extent, by imposing a subcritical CCF boundary condition at the lower end, $z=0$, of the annulus, and by applying a spatial ramp, $\epsilon(z)$, of the driving that starts at a subcritical value, $\epsilon(z=0)=-\epsilon_0$, and joins smoothly to a supercritical plateau, $\epsilon(z\geq 12d)=\epsilon_0$.

In the following, we list briefly the main properties of propagating TVF fronts in the driving range $0.01\leq\epsilon_0\leq 0.1$ and in the range of radius ratios $0.5066\leq\eta\leq 0.893$ investigated in this work.

(1) They are circular symmetric, flat, and they propagate at a right angle to the cylinder axes from an end into the annulus.

(2) Their velocities c are very close[14] to the prediction $c_A=2(\epsilon_0)^{1/2}\xi_0/\tau_0$ of Aronson and Weinberger[25] derived from the lowest-order amplitude equation. Furthermore, c is practically independent of η—ξ_0/τ_0 varies only about 1%.

(3) The axial profiles of the TVF intensities are quite similar to the universal front solutions that we obtained in this work from the amplitude equation for propagation velocities c_A. In accordance with this result, our front extensions l are almost independent of η and show a variation with the driving proportional to $\epsilon_0^{-1/2}$. However, our fronts are consistently steeper by about 20%. The front extension for $\epsilon_0=0.1$, e.g., is about $2.2d$, so that the TVF intensity varies on the wavelength scale. Nevertheless, the amplitude equation being derived under the assumption of slow spatial variation of the TVF intensity reproduces the propagation velocity and the front profile reasonably well.

(4) As the TVF intensity increases in the front, so do the differences between the large axial extension Δ_{in} of slow radial inflow and the small axial extension Δ_{out} of fast radial outflow. Thus the flow pattern unraveled by the propagating front agrees with that of the lowest-order amplitude equation ($\Delta_{\text{in}}=\Delta_{\text{out}}$, $u_{\text{in}}=u_{\text{out}}$) only in the extreme precursing head of the front. With growing intensity along the front, the ratios $u_{\text{in}}/u_{\text{out}}$ of inflow and outflow maxima smoothly decrease, while the ratios $\Delta_{\text{in}}/\Delta_{\text{out}}$ simultaneously increase to the bulk values which differ, e.g., for $\epsilon_0=0.1$, by about 30% from unity. The local wavelength $\Delta_{\text{in}}+\Delta_{\text{out}}$, however, does not vary appreciably in the front. It is close to that with the largest vortex growth rate obtained in a linear stability analysis of CCF.

ACKNOWLEDGMENT

Discussions with G. Ahlers are gratefully acknowledged.

APPENDIX: NUMERICAL SOLUTION OF THE NAVIER-STOKES EQUATIONS

Here we present some details of our numerical procedure to solve the Navier-Stokes equations.

1. The equations

First, we rewrite the momentum balance (2.1a) with the help of the incompressibility condition

$$D=\vec{\nabla}\cdot\vec{u}=0 \tag{A1a}$$

in the "conservative" form

$$\partial_t\vec{u}=-\vec{\nabla}\cdot(\vec{u}\,\vec{u})-\vec{\nabla}p/\rho-\nu\vec{\nabla}\times(\vec{\nabla}\times\vec{u})\ . \tag{A1b}$$

Here, $(\vec{u}\,\vec{u})$ denotes a dyad. Equations (A1) and (2.1) are equivalent to each other. However, after discretization in cylindrical geometry on a spatial lattice, discussed further below, only (A1b) ensures[28] a correct momentum balance. Therefore our simulation is based upon (A1), together with the Poisson equation for the dynamic pressure,

$$\nabla^2 p/\rho=-\partial_t D-\vec{\nabla}\cdot[\vec{\nabla}\cdot(\vec{u}\,\vec{u})]\ , \tag{A1c}$$

derived from taking the divergence of (A1b). Here we have kept the term $\partial_t D$ which vanishes in the continuum version (A1a) of the mass-conservation law. However, solving (A1) approximately on a lattice in space and time, one must retain[28] the discretized version of $\partial_t D$ even

though the appropriate restrictions aiming at $D=0$ are enforced. In an aside, we mention that in the Poisson equation derived from (2.1a) there would appear, in addition to an advective contribution, the diffusive term $\nu\nabla^2 D$. Its absence in (A1c) entails a simpler discretized form, and thus reduction of round-off-error accumulation.

For rotationally invariant flows considered in this work, the momentum-balance equations (A1b) read

$$\partial_t u+\frac{1}{r}\partial_r(ru^2)-\frac{v^2}{r}+\partial_z(uw)=-\partial_r p/\rho-\nu\partial_z(\partial_r w-\partial_z u)\ , \tag{A2a}$$

$$\partial_t v+\frac{1}{r}\partial_r(ruv)+\frac{uv}{r}+\partial_z(vw)=\nu\partial_z^2 v+\nu\partial_r\left[\frac{1}{r}\partial_r(rv)\right]\ , \tag{A2b}$$

$$\partial_t w+\frac{1}{r}\partial_r(ruw)+\partial_z w^2=-\partial_z p/\rho+\frac{\nu}{r}\partial_r(r\partial_r w-r\partial_w u)\ . \tag{A2c}$$

The Poisson equation has the form

$$\partial_z^2 p/\rho+\frac{1}{r}(r\partial_r p)/\rho=-\frac{1}{r}\partial_r^2(ru^2)-\partial_z^2 w^2-2\partial_r\partial_z(uw)+\frac{1}{r}\partial_r v^2-\frac{2}{r}\partial_z(uw)-\partial_t D\ , \tag{A3}$$

and

$$D=\frac{1}{r}\partial_r(ru)+\partial_z w\ . \tag{A4}$$

2. Numerical procedure

We have solved Eqs. (A2)—(A4) on a lattice with an explicit finite-difference method[28] using forward differences for ∂_t and central differences for spatial derivatives. The numerical procedure is as follows: Given the velocity field at time t_n, we determine the pressure $p(t_n)$ by solving the discretized version of the Poisson equation (A3) iteratively by successive over-relaxation. In order to obtain good start values for the iteration, we extrapolate, with orthogonal polynomials, the previously determined pressures $p(t_m<t_n)$. This can reduce the number of iterations by roughly a factor of 3, in comparison to unextrapolated start values $p(t_{n-1})$. The rate of change of D entering (A3) is approximated by $-D(t_n)/\Delta t$, thus imposing the incompressibility restriction via $D(t_{n+1})=0$. Having determined $p(t_n)$, we obtain the velocity field at time t_{n+1} by a forward time step of (A2).

Results reported here were obtained on uniform lattices (cf. next subsection) with a spacing between like points of $\Delta r=\Delta z=0.05d$ using a time step $\Delta t\simeq 3.4\times 10^{-3}\tau$. Such a time step required about 1.6 sec central-processing-unit (CPU) time on an IBM 3033 computer in our flow simulation, in annuli of aspect ratio $\Gamma=25$.

3. The lattice

Our lattice in the r-z plane consists of three interlacing sublattices as shown schematically in Fig. 15. One (●) for the radial velocity u, one (■) for the axial velocity w, and one (×) for the tangential velocity v and pressure p. This lattice structure enforces[28] correct momentum balance of the discretized equations (A2) for every cell indicated by thin solid lines in Fig. 15.

The position of the lattice points and their spacings are chosen such that the fluid boundaries lie halfway between pressure points (×). Thus the top and bottom boundaries of the annulus (marked, in Fig, 15, by the thick solid horizontal line and the small dots, respectively) go through w points (■). The vertical boundaries at r_1 and r_2 (marked by the dashed line and the thick solid vertical line, respectively) go through u points (●). Note that there is one layer of lattice points outside the annulus, as indicated in Fig. 15.

4. Boundary conditions

The fluid velocity is prescribed on the boundaries of the annulus. This is done in two different ways: (i) At those points lying on a boundary, we fix the corresponding velocity component to have the desired value, e.g., $u(\bullet)=0$ at $r=r_1,r_2$; (ii) for those components for which the lattice points do not fall on a boundary, we force the average over the two points on either side of the boundary to have

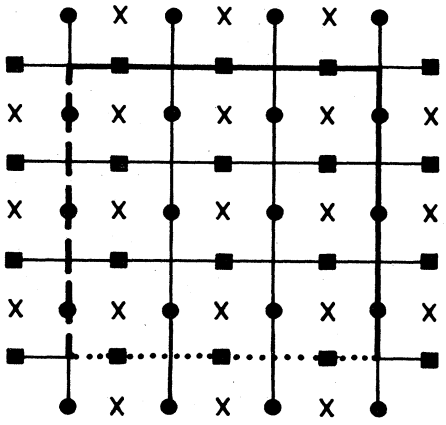

FIG. 15. Schematic structure of the discretization lattices in an r-z section of the annulus for the radial velocity u (large dots), axial velocity w (squares), and tangential velocity v, together with the pressure p (crosses). Thick solid vertical and horizontal lines denote the outer cylinder at r_2 and the top boundary at $z=\Gamma d$, respectively. Dashed line represents the inner boundary at $r=r_1$ and dotted line marks the bottom boundary at $z=0$.

the desired value by adjusting the velocity at the outside points appropriately.

In this work the velocity field vanishes at the outer cylinder, $r=r_2$, and at the top end, $z=\Gamma d$, of the annulus. At the inner "cylinder," $r=r_1$, we force the radial and axial velocity to vanish, $u=w=0$, and the tangential velocity, $v(r_1,z)$, to have the axial profile discussed in Sec. III B. At the lower end, $z=0$, of the annulus, we have $u=w=0$ and a CCF profile for the tangential velocity $v(r,z=0)$.

Theoretical problems would arise for our setup with the continuous NSE's from the discontinuity of the boundary conditions at the corner, $r=r_1$ and $z=\Gamma d$, between the rotating inner cylinder and the stationary top plate (at the lower corner, $r=r_1$ and $z=0$, there would be not discontinuity in our case). However, for the discretized NSE's on the lattice shown in Fig. 15, this problem practically does not show up[29] for the lattice spacing used here.

*Permanent address.

[1]R. C. Di Prima and H. L. Swinney, in *Hydrodynamic Instabilities and the Transition to Turbulence,* edited by H. L. Swinney and J. P. Gollub (Springer, Berlin, 1981).

[2]E. L. Koschmieder, in *Advances in Chemical Physics,* edited by I. Prigogine and S. A. Rice (Interscience, New York, 1973), Vol. 26, p. 177.

[3]J. S. Langer and H. Müller-Krumbhaar, Acta Metall. **26**, 1681 (1978); **26**, 1689 (1978); **26**, 1697 (1978).

[4]C. Vidal and A. Pacault, in *Evolution of Order and Chaos,* edited by H. Haken (Springer, Berlin, 1982), p. 74.

[5]A. Schlüter, D. Lortz, and F. Busse, J. Fluid Mech. **23**, 129 (1965).

[6]S. Kogelmann and R. C. Di Prima, Phys. Fluids **13**, 1 (1970).

[7]G. Ahlers and D. S. Cannell, in *Synergetics—From Microscopic to Macroscopic Order,* edited by E. Frehland and H. Haken (Springer, Berlin, 1983).

[8]L. Kramer, E. Ben-Jacob, H. Brand, and M. C. Cross, Phys. Rev. Lett. **49**, 1891 (1982).

[9]D. S. Cannell, M. A. Dominguez-Lerma, and G. Ahlers, Phys. Rev. Lett. **50**, 1365 (1983), and unpublished.

[10]This agrees with preliminary numerical results obtained by us under slightly different conditions.

[11]J. S. Langer, Rev. Mod. Phys. **52**, 1 (1980).

[12]G. I. Sivashinsky, Ann. Rev. Fluid Mech. **15**, 179 (1983).

[13]G. Ahlers and D. S. Cannell, Phys. Rev. Lett. **50**, 1583 (1983), and unpublished.

[14]M. Lücke, M. Mihelcic, and K. Wingerath, Phys. Rev. Lett. **52**, 625 (1984).

[15]G. P. Neitzel, J. Fluid Mech. **141**, 51 (1984).

[16]M. Lücke, M. Mihelcic, and K. Wingerath (unpublished).

[17]G. Pfister and I. Rehberg, Phys. Lett. **83A**, 19 (1981).

[18]G. K. Batchelor, *An Introduction to Fluid Dynamics* (Cambridge University Press, Cambridge, 1967).

[19]C. F. Chen and R. P. Kirchner, J. Fluid Mech. **48**, 365 (1971).

[20]C. J. Tranter, *Integral Transforms in Mathematical Physics* (Wiley, New York, 1956).

[21]See, e.g., R. Graham and J. A. Domaradzki, Phys. Rev. A **26**, 1572 (1982), and references cited therein.

[22]A. Davey, J. Fluid Mech. **14**, 336 (1962).

[23]M. A. Dominguez-Lerma, G. Ahlers, and D. S. Cannell, Phys. Fluids **27**, 856 (1984).

[24]G. Dee and J. S. Langer, Phys. Rev. Lett. **50**, 383 (1983).

[25]D. G. Aronson and H. F. Weinberger, *Advances in Mathematics* (Academic, New York, 1978), Vol. 30, p. 33.

[26]J. P. Gollub and Michael H. Freilich, Phys. Fluids **19**, 618 (1976).

[27]H. A. Snyder, J. Fluid Mech. **35**, 273 (1969).

[28]J. E. Welch, F. H. Harlow, J. P. Shannon, and B. J. Daly, Los Alamos Scientific Laboratory Report No. LA-3425, 1966 (unpublished).

[29]For a more detailed discussion, see M. Lücke, M. Mihelcic, K. Wingerath, and G. Pfister, J. Fluid Mech. **140**, 343 (1984).